RSC Advances

PAPER

View Article Online
View Journal | View Issue

Cite this: *RSC Adv.*, 2021, **11**, 10785

Surface chemical functionality of carbon dots: influence on the structure and energy storage performance of the layered double hydroxide

Huimin Li,[a] Yingjun Xie,[a] Yingliang Liu,[a] Yong Xiao,[a] Hang Hu,[a] Yeru Liang *[a] and Mingtao Zheng *[ab]

As a kind of zero-dimensional material, carbon dots (CDs) have become a kind of promising novel material due to their incomparable unique physical and chemical properties. Despite the optical properties of CDs being widely studied, their surface chemical functions are rarely reported. Here we propose an interesting insight into the important role of surface chemical properties of CDs in adjusting the structure of the layered double hydroxide (LDH) and its energy storage performance. It was demonstrated that CDs with positive charge (p-CDs) not only reduce the size of the flower-like LDH through affecting the growth of LDH sheets, but also act as a structure stabilizer. After calcination, the layered double oxide (LDO) maintained the morphology of the LDH and prevented the stacking of layers. And the superiority of the composite in lithium-ion batteries (LIBs) was demonstrated. When used as an anode of LIBs, composites possess outstanding specific capacity, cycle stability and rate performance. It presents the discharge capacity of 1182 mA h g^{-1} and capacity retention of 94% at the current density of 100 mA g^{-1} after 100 cycles. Our work demonstrates the important chemical functions of CDs and expands their future applications.

Received 27th January 2021
Accepted 3rd March 2021

DOI: 10.1039/d1ra00706h

rsc.li/rsc-advances

1. Introduction

As a new zero-dimensional carbon-based material, carbon dots (CDs) have attracted much attention because of their excellent properties such as good water solubility, environmental friendliness, low toxicity and wide source of raw materials.[1,2] They possess abundant surface functional groups and amorphous or nanocrystalline cores with dimensions below 10 nm.[3] Since the discovery of CDs, various methods have been used to prepare the functional material, such as laser ablation, arc discharge, microwave synthesis, hydrothermal method and so on.[4,5] While the optical properties of CDs including fluorescence,[6] phosphorescence,[7] up-conversion luminescence,[8] and near-infrared luminescence[9] were largely studied, their chemical functions are rarely reported.

Recently, some prospective studies have shown the great potential value of the chemical functions of CDs. Compared with other template regulators, CDs are non-toxic, easily removed and low cost.[10,11] Because the surface of the CDs carries a large number of groups, they can achieve surface wettability and firmly adhere to inorganic materials.[12–14] Then they induce and control the composite material through various groups on the surface, changing its size and even shape. It has been found that CDs can induce materials to form different morphology (*e.g.*, flower,[15,16] sphere[17] and tremella[18]) to tailor their physical and chemical properties, thus meeting specific requirements. In addition, the chemical surface properties of CDs can be adjusted by doping various heteroatoms, such as N, F, B, S and Mg to improve their performance.[19–23] It has been demonstrated that the CDs attached to the composites can not only increase the ion transport interface between the electrode and electrolyte, but also improve the conductivity of the composite material through edge effect and quantum constraint, effectively improving the specific capacitance and specific capacity, as well as cycling stability.[24,25] For example, Hou *et al.* synthesized carbon quantum dots (CQDs) and their derivative 3D porous carbon frameworks and applied them to sodium ion batteries, which had a long cycle life and excellent multiplier performance.[26] Lv *et al.* synthesized CDs-induced MnO_2 nanowires to enhance the wettability between electrode and electrolyte, thus delivering high specific capacitance and good stability.[27] Despite the above progresses, the diversity of CDs in tailoring structure and performance still needs to be further explored.

In this work, we propose an interesting insight into the important role of surface chemical functions of CDs in adjusting the nanostructure of layered double hydroxide (LDH) and its energy storage performance. It is found that as a structural regulator, CDs could use their positively charged properties to

[a]*Key Laboratory for Biobased Materials and Energy of Ministry of Education/Guangdong Provincial Engineering Technology Research Center for Optical Agriculture, College of Materials and Energy, South China Agricultural University, Guangzhou, 510642, China. E-mail: liangyr@scau.edu.cn; mtzheng@scau.edu.cn*

[b]*Maoming Branch, Guangdong Laboratory for Modern Agriculture, Maoming 525000, China*

hinder the growth of LDH sheets, thereby inducing smaller flower-like structure, which is conductive to shortening the rate of ion conduction. Compared with the template method and chemical deposition method commonly used in other work, this method has the advantages of low cost and simple operation. After calcination, LDO/p-CDs composite exhibited a high discharge capacity of 1182 mA h g^{-1} and capacity retention of 94% at the current density of 100 mA g^{-1} after 100 cycles. These outstanding performances were derived from the high surface area, suitable nanostructure and unique three-dimensional morphology of composites. This work not only provides the chemical regulation effect of CDs, but also offers new insights on energy storage.

2. Experimental section

2.1. Materials

$NiCl_2 \cdot 6H_2O$, $MnCl_2$, NH_4F was purchased from Macklin Biochemical Co., Ltd. (Shanghai, China). Hexamethylene tetramine and ethylenediamine (EDA) was obtained from Guangzhou Chemical Reagent Factory. Citric acid monohydrate was procured from Shanghai Lingfeng Chemical Reagent Co., Ltd. (China). Ethanolamine (EA) was obtained from Tianjin Fuyu Fine Chemical Co., Ltd. (China).

2.2. Preparation of p-CDs

2.1 g citric acid monohydrate and 482 μl EA were dissolved into 20 ml deionized water at room temperature. The solution was mixed thoroughly by ultrasonication for 30 min. Then the uniform solution was put into the Teflon-lined stainless-steeled autoclave with heating 4 h at 200 °C, hence producing the p-CDs solution.

2.3. Preparation of n-CDs

The preparation of n-CDs was based on Zhu's study.[28] 0.42 g citric acid monohydrate and 536 μl EDA were added into a 30 ml Teflon-lined stainless-steel autoclave, with the increase of 10 ml water. After heating 5 h at 200 °C, the autoclave was cooled down to room temperature. Finally, the CDs solution was dialyzed in a length of dialysis bag with 1000 ml deionized water for 3 d and the water was changed every 24 h.

2.4. Synthesis of LDO/CDs

For synthesis of layered double oxides (LDO), hydrothermal reaction and calcination treatment were used in this process. The molar ratio of Ni^{2+}/Mn^{2+} was 3 : 1. In a typical course, 0.75 mmol $NiCl_2 \cdot 6H_2O$ and 0.25 mmol $MnCl_2$ were dissolved in 60 ml deionized water. 1.25 mmol NH_4F, 1 mmol hexamethylene tetramine and 2 ml CDs were put into the above salt solution under stirring. At the same time, the liquid was treated with N_2 for half an hour. After that, the mixed solution was transferred into a 100 ml Teflon-lined stainless steel autoclave and kept at 100 °C for 12 h. The sediments were obtained after centrifugation, washing by water and vacuum-drying overnight. The NiMn–LDH/CDs was obtained. Then the sediments were put into the porcelain crucible and heated at 400 °C for 2 h in air by a heating rate of 2 °C min^{-1} to acquire the LDO/CDs. The preparation process of LDO was as same as LDO/CDs, excepting the addition of CDs. According to the variety of CDs, the products were labeled as LDO/p-CDs and LDO/n-CDs.

2.5. Characterization

The morphology and microstructure of LDO, LDO/p-CDs and LDO/n-CDs were characterized by the high-resolution transmission electron microscope (HRTEM, Thermo Fisher Talos F200S) and the field emission scanning electron microscope (FESEM, ZEISS Ultra 55). The crystal phase of the samples was measured by X-ray diffraction (XRD, XD-2X/M4600, Cu Kα radiation, λ = 0.154051 nm). N_2 adsorption–desorption isotherms were measured at 77 K from 3Flex (Micromeritics, America). SSAs were calculated by the Brunauer–Emmett–Teller (BET) model. For each sample, functional groups in the range of 400–4000 cm^{-1} were obtained from KBr tablets using a Fourier transform infrared spectrum (FT-IR, Nicolet Nexus 410). The content and composition of elements are measured by X-ray photoelectron spectroscopy (XPS, Thermo Scientific ESCALAB 250Xi).

2.6. Electrochemical measurements

Standard CR2032 coin-type cells were obtained by assembling a half cell in a nitrogen-protected glovebox. The samples, acetylene black and PVDF were uniformly mixed in *N*-methyl pyrrolidone with a mass ratio of 7 : 2 : 1 to prepare the working electrodes, then the slurry was covered copper foil. The working electrodes were dried at 60 °C under vacuum. The loading capacity of the active substance for each copper foil was about 1 mg. Using 1 M $LiPF_6$ in ethylene carbonate : dimethyl carbonate (1 : 1 (v/v)) as electrolyte, Celgard 2400 as the isolator and lithium sheet as counter electrode when assembling coin-type cells. The oxygen and water content in the glovebox were less than 1 ppm. The electrochemical performance was estimated at different current densities in the voltage between 0.01 and 3.0 V *vs.* Li/Li^+ (Neware, BTS-5 V/10 mA). Cyclic voltammetry (CV) measurements were tested by CHI-760E electrochemical workstation at the scan rate of 0.1 mV s^{-1}. Electrochemical impedance spectroscopy (EIS) was performed on the electrochemical system (Zahnex Corp.) in the frequency range of 0.01 Hz to 100 kHz at an amplitude of 5 mV.

3. Results and discussions

Initially, $NiCl_2 \cdot 6H_2O$ and $MnCl_2$ solutions containing CDs are mixed in N_2 atmosphere. Then, the LDH/CDs hybrid solution is prepared by hydrothermal method. In order to highlight the influence of the surface chemistry of CDs on the structure, positively charged p-CDs and negatively charged n-CDs are introduced. The hybrids prepared with the two CDs are named LDH/p-CDs and LDH/n-CDs, respectively. For comparison, LDH material is obtained by the same method without adding CDs. During the hydrothermal process, CDs are attached to the petals of the flower. The addition of n-CDs will not hinder the growth of LDH slices (Fig. 1b), and the size of the resulting flower-like

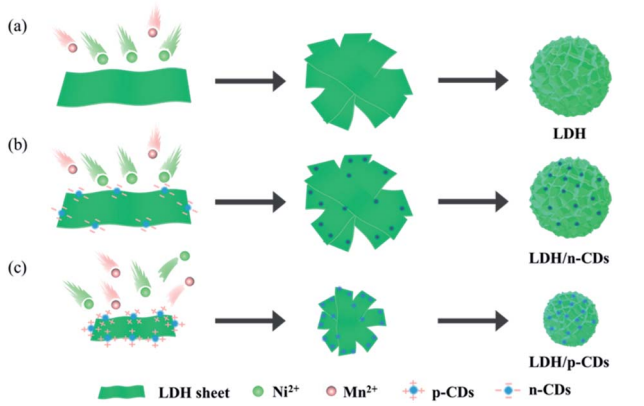

Fig. 1 Illustration of the formation of (a) LDH, (b) LDH/n-CDs, and (c) LDH/p-CDs.

spheres is similar to that of the control group without CDs (Fig. 1a). However, the addition of p-CDs will prevent the aggregation of Ni^{2+} and Mn^{2+} and hinder the growth of LDH sheets, leading to the reduction of size, which will reduce the size of the flower-like spheres after assembly, too (Fig. 1c). Finally, LDO, LDO/p-CDs and LDO/n-CDs are obtained by calcination and applied as anode material for lithium ion batteries. It is found that LDO/p-CDs with smaller size have the best performance.

Both p-CDs and n-CDs exhibit blue fluorescence under 365 nm UV-lamp irradiation (inset of Fig. 3a and b) and this luminescence disappears immediately without UV-lamp. In the sunlight, p-CDs are yellow and n-CDs are transparent colorless. Fig. 3a and b shows photoluminescence spectra of p-CDs and n-CDs. Fig. 3c display zeta potential of two kinds of CDs. p-CDs has positive charge and n-CDs has negative charge. As shown in Fig. 2d and e, the nanoparticle sizes of p-CDs and n-CDs are respectively 3.5–8 nm and 3.5–7.5 nm with average diameters of about 5.54 nm and 5.22 nm. To further explore the property of p-CDs and n-CDs, XPS high-resolution spectra are introduced to analyze. High resolution C 1s spectra (Fig. 3a) show that p-CDs contain C=O bond (288.5 eV), C–O bond (286.7 eV), C–N bond (285.8 eV), and C=C bond (284.6 eV) functional groups. And

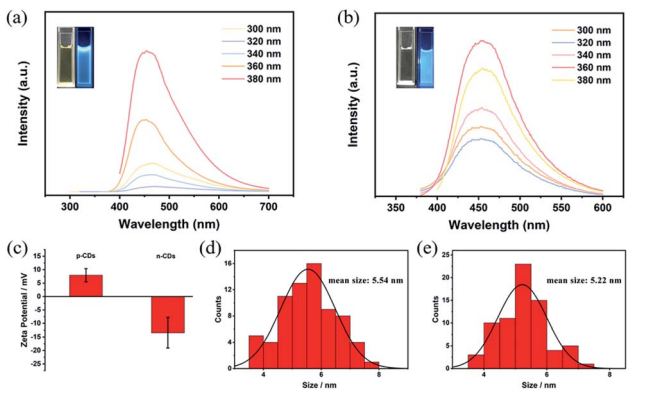

Fig. 2 Fluorescence (FL) excitation of (a) p-CDs and (b) n-CDs, zeta potential of (c) p-CDs and n-CDs. (d) and (e) show the size distributions of p-CDs and n-CDs, respectively.

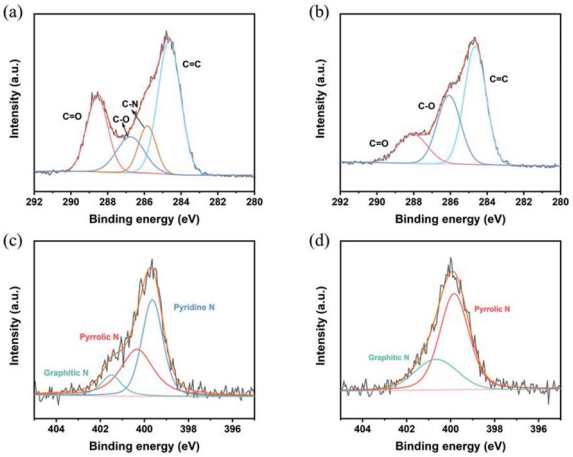

Fig. 3 High-resolution XPS spectra of C 1s and N 1s for (a and c) p-CDs, (b and d) n-CDs.

the N 1s spectra of p-CDs (Fig. 3c) is divided into three peaks with binding energy of 399.3 eV, 400.4 eV and 401.5 eV, corresponding to pyridine N, pyrrolic N and graphitic N, respectively. To compare the differences between p-CDs and n-CDs, the high-resolution C 1s and N 1s spectra is also displayed in Fig. 3b and d. For the C 1s spectra of n-CDs (Fig. 3b), there are three peaks including C=C bonds, C–O bonds and C=O bonds. As displayed in Fig. 3d, the high-resolution spectrum of N 1s is divided into two peaks, corresponding to graphitic-N and pyrrolic-N groups. However, it can be observed that a significant increase for pyridine N structure in high-resolution N 1s spectra of p-CDs. This indicates that the positive charge of p-CDs is possibly caused by the formation of the pyridine N and pyrrolic N, which is in good agreement with the zeta-potential results.[29]

Fig. 4a shows the flower-like spheres morphology of LDH. The size of flower is 3–4 μm. The petals of the flower are relatively smooth as displayed in Fig. 4d. But when p-CDs are added, the size of LDH shrinks to the nanometer level. The size

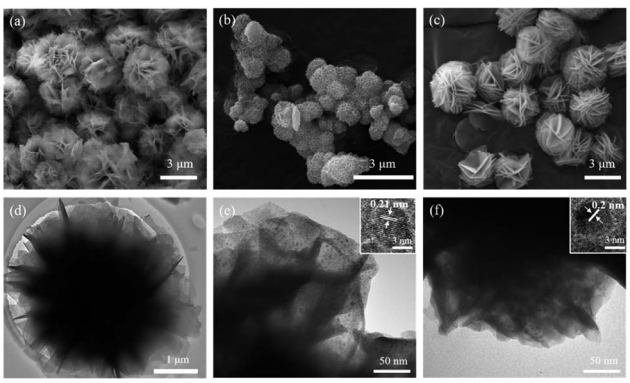

Fig. 4 Morphology characterizations of LDH, LDH/pCDs and LDH/n-CDs. (a) SEM image and (d) TEM image of LDH. (b) SEM image and (e) TEM image of LDH/p-CDs. (c) SEM image and (f) TEM image of LDH/n-CDs. The insets in (e) and (f) are the lattice of p-CDs and n-CDs, respectively.

of LDH/p-CDs has been reduced to 500–600 nm (Fig. 4b), which is smaller than LDH. LDH/p-CDs tend to aggregate together and its boundaries are not obvious. As shown in TEM image (Fig. 4e), p-CDs are evenly distributed on the petals and its lattice spacing is about 0.21 nm (inset in Fig. 4e). However, the size of LDH/n-CDs is about 3 μm which is as same as LDH. It illustrates that the addition of CDs with negative charge does not change the size of LDH. As shown in Fig. 4f, n-CDs are attached to LDH uniformly and its lattice spacing is about 0.2 nm (inset in Fig. 4f). Herein, there is a possible reason for the synthesis of the smaller LDH that p-CDs act as a surfactant during the nucleation and growth of LDH, preventing further growth of LDH sheets and assembly into micron-sized flowers.[30–32] When CDs are introduced into the reaction, they will be overlaid on the petals of LDH. CDs with positive charge has a greater inhibitory effect on the anisotropic growth of the LDH crystal than CDs with negative charge. The growth of nanosheets is hindered, and finally the size of flower is reduced. LDH/p-CDs with smaller size can exhibit higher surface activity, faster ion and electron conduction, and more stable mechanical properties.[33–37]

After calcination in the air, the morphology characterization of LDO, LDO/p-CDs and LDO/n-CDs are to a great extent preserved. The size of LDO (Fig. 5a) and LDO/n-CDs (Fig. 5c) are still about 3 μm and p-CDs (Fig. 5b) are still about 600 nm. It's worth noting that the petals of flower have a little breakage after calcination. It means that the LDH nanosheets that make up the petals react with oxygen to form LDO. So that some of the components of the nanosheets disappear because of the reaction, and this also can be seen from the TEM images of the three samples. At the same time, it clearly shows that there are no CDs on the petals after calcination (Fig. 5d–f). TEM images show that the petals are not smooth but rather granular. Fig. 5h–j display the elemental mapping images of partial region in Fig. 5g. It's obvious that the elements of O, Ni and Mn are uniformly dispersed on the nanosheets.

Fig. 6a shows the XRD patterns of LDO, LDO/p-CDs and LDO/n-CDs. It can be seen that the sharp and intense characteristic diffraction peaks of three samples at 2θ degree of 37.1°, 43.2°, 63.0°, 75.1°, and 79.6° are corresponded to the (222), (400), (440), (533), (444) diffraction planes, respectively, for Ni_6MnO_8 (JCPDS no. 42-0479). Whether CDs are added or not, LDO will be formed after calcination. The result indicates the successful synthesis of LDO. In addition, with adding p-CDs, the diffraction peaks of sample are broadened and the intensity decreased, indicating the gradual decreasing of crystal size.[38] This can also provide additional electrochemical active sites. Before calcination, LDH, LDH/p-CDs and LDH/n-CDs are analyzed by TG. Fig. 6b shows the weight loss of three samples under air at a scan rate of 10 °C min^{-1} below 600 °C. When the temperature rises to 600 °C, the weight of LDH droop to 68.28%, LDH/n-CDs droop to 61.58% and LDH/p-CDs unexpectedly droop to 43.65%. LDH/p-CDs start and end oxidation (the steepest part of the curve) at lower temperatures than LDH and LDH/n-CDs. This is because there are many holes and a variety of functional groups in the surface of the CDs, and they have a strong hygroscopicity, which can effectively capture more water molecules in it. Under the same quality, LDH added with CDs contains more water molecules. Compared with LDH without CDs, LDH/n-CDs and LDH/p-CDs lose more weight at higher temperature. In addition, due to the smaller size and larger surface area (Fig. 6c) of LDH/p-CDs, the contact area of CDs and water molecules is increased, resulting in more captured water molecules than LDH/n-CDs. Nitrogen adsorption/desorption isotherms display the properties of surface area. As shown in Fig. 6c, the three isotherms can be identified as type-IV. Calculating by Brunauer–Emmett–Teller (BET) model, the specific surface area of LDO, LDO/n-CDs and LDO/p-CDs are 32.68, 35.75, and 63.89 $m^2 g^{-1}$, respectively. The smaller size promotes the BET increase of the material. Inset of Fig. 6c shows the pore size distribution of the samples. After calcination, the pore size of LDO, LDO/n-CDs and LDO/p-CDs is

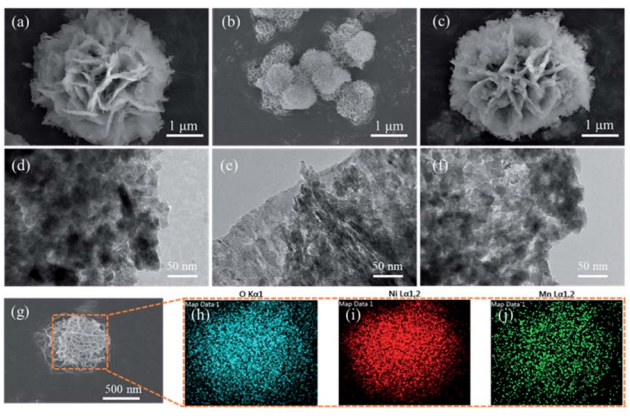

Fig. 5 Morphology characterizations after calcination. SEM images of (a) LDO, (b) LDO/p-CDs, (c) LDO/n-CDs. TEM images of (d) LDO, (e) LDO/p-CDs, (f) LDO/n-CDs. (g–j) Elemental mapping images of LDO/p-CDs.

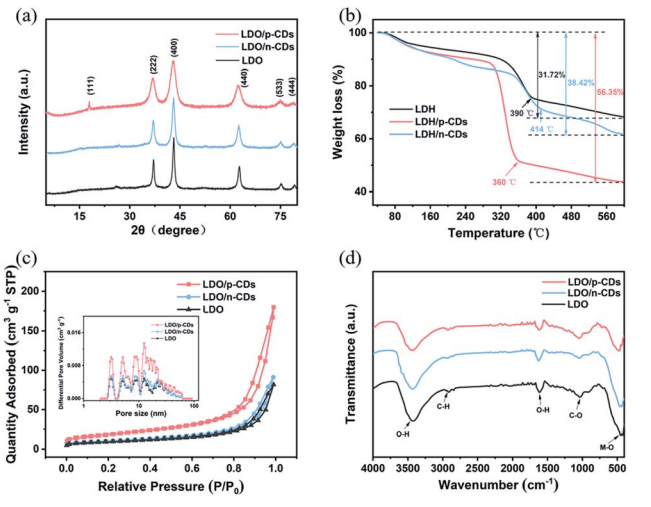

Fig. 6 (a) XRD patterns of LDO, LDO/p-CDs, LDO/n-CDs. (b) TG curves under air at a scan rate of 10 °C min^{-1} of LDH, LDH/p-CDs and LDH/n-CDs. (c) Nitrogen adsorption/desorption isotherms (the inset shows the pore size distribution), (d) FT-IR spectra of LDO, LDO/p-CDs and LDO/n-CDs measured from 400–4000 cm^{-1}.

approximately the same, which is mainly distributed in mesopores with very few macropore. However, the results show that both the mesopore volume and the mesopore area of LDO/p-CDs are higher than other two samples. In general, large specific surface area can provide sufficient adsorption sites.[39–41] At the same time, the increase in the number of pores and volume of the sample makes it contact with the electrolyte adequately, which can promote the improvement of electrochemical performance. This may be one reason for the difference in electrochemical properties.

FT-IR analysis is further carried out to verify the functional group of the samples in the region of 400–4000 cm^{-1}. Fig. 6d represents the characteristic peaks of LDO, LDO/p-CDs and LDO/n-CDs. Upon treatment with calcination in air, the intensities of the characteristic peaks corresponding to the metal functionalities, such as the adsorption bands of M–O at 463 cm^{-1}, which is caused by the cation–oxygen vibrations. In these spectra, we can see a broad adsorption in the range of 3250–3550 cm^{-1} and an adsorption at 1624 cm^{-1}, which are originated from the hydrogen bonding in LDO or the ν-OH mode of adsorption hydroxyl groups in water molecules. The peak at 2926 cm^{-1} is caused by the stretching vibration of C–H on saturation C and the peak at 1038 cm^{-1} is ascribed to the stretching vibration of C–O.

In addition, X-ray photoelectron spectroscopy (XPS) is used to further characterize the LDO oxidation state. Fig. 7a shows the XPS full spectra of three samples. All three of them have Ni, Mn, C, O elements, which is consistent with the result of element mapping. The Ni 2p and Mn 2p peaks are observed at 856.4 eV and 643.4 eV, respectively. And 530.5 eV and 285.6 eV correspond to O 1s and C 1s peaks. The XPS spectra has a week C 1s signal, indicating that Ni, Mn and O elements mainly exist in the LDO. Fig. 7b–d exhibits the high-resolution Ni 2p, Mn 2p and O 1s XPS spectra of LDO/p-CDs. After the refined fitting, the Ni 2p spectrum (Fig. 7b) is composed of four peaks. The fitted peaks of Ni $2p_{1/2}$ at 873.1 eV and Ni $2p_{3/2}$ at 855.4 eV are corresponded to Ni^{2+}, while the peaks at 879.8 eV and 861.4 eV are attributed to Ni^{3+}.[42,43] The Mn 2p spectrum (Fig. 7c) clearly evidences the presence of two peaks at 653.7 eV and 642.8 eV, which are corresponding to Mn $2p_{1/2}$ and Mn $2p_{3/2}$, indicating the existence of Mn^{3+} in the LDO/p-CDs.[44–48] Fig. 6d exhibits the O 1s spectrum fitted with two peaks, which are located at 531.5 eV and 529.9 eV. The peak at 529.9 eV is the characteristic peak of metal–oxygen bond. The fitted peak located at 531.5 eV is associated with metal–OH bond, which is considered to be an oxide defect on the surface of the sample.[44,49,50] The presence of the O 1s peak indicates the oxidation of the powder after exposure to the air. The XPS results reveal the successful preparation of LDO material.

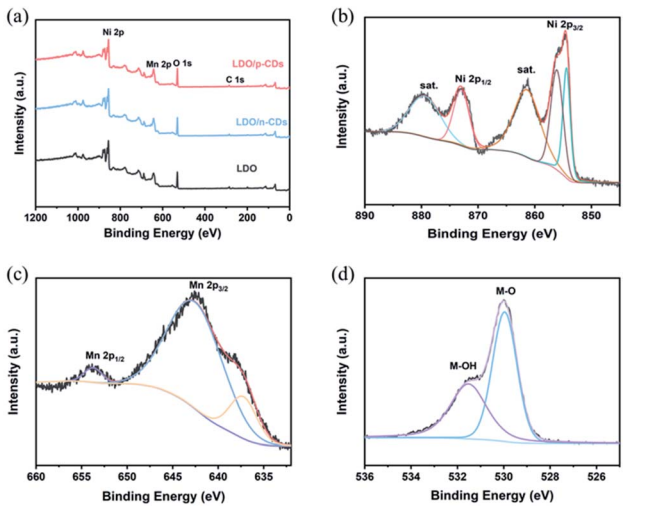

Fig. 7 (a) XPS survey spectrum of LDO, LDO/n-CDs and LDO/p-CDs; high-resolution spectrum of LDO/p-CDs: (b) Ni 2p; (c) Mn 2p; (d) O 1s.

Based on the above results of XRD, SEM, N_2 adsorption/desorption isotherms, FT-IR spectra, XPS and TG, it is found that the LDO regulated by p-CDs is significantly different from LDO/n-CDs and LDO. LDO/p-CDs has a smaller size and a higher specific surface area. Its structural and compositional characteristics are expected to enhance electrochemical properties.

The electrochemical properties of three prepared samples are studied as anode materials for lithium ion batteries. As can be seen from Fig. 8a–c, they display the first four CV curves of LDO, LDO/p-CDs and LDO/n-CDs at the scanning rate of 0.1 mV s^{-1} over the voltage window of 0.01–3 V. In the first cycle, the cathode reduction peaks at about 0.38 V and 0.5 V are attributed to the formation of solid electrolyte interphase (SEI) films and decomposition of electrolyte. At that point Li^+ is inserted irreversibly and then it forms Li_2O. Two wide oxidation peaks at 1.52 V and 2.24 V correspond to the oxidation of metal Mn to Mn^{2+} and Ni to Ni^{2+}, respectively. A new reduction peak appears from the second cycle. The reduction peak at about 0.82 V represents the reduction of Mn^{2+} to Mn and Ni^{2+} to Ni. From this, we can infer that the electrochemical equation of Ni_6MnO_8 in lithium ion battery is as follows:[51]

$$Ni_6MnO_8 + 16Li^+ + 16e^- \rightarrow 6Ni + Mn + 8Li_2O \quad (1)$$

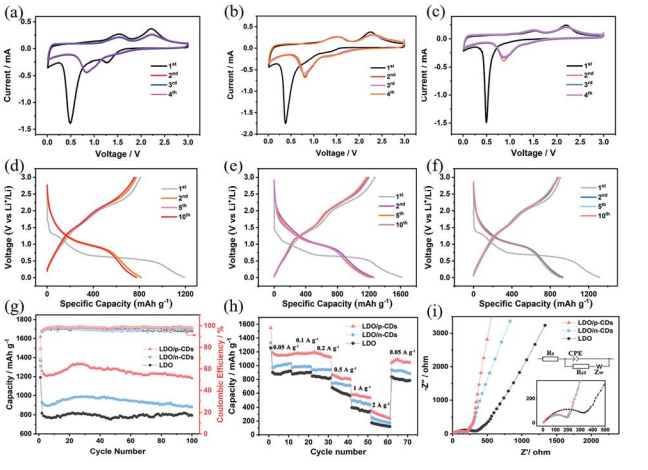

Fig. 8 CV curves of (a) LDO, (b) LDO/p-CDs and (c) LDO/n-CDs at a scan rate of 0.1 mV s^{-1} over a potential range of 0.01–3 V; galvanostatic charge–discharge profiles of (d) LDO, (e) LDO/p-CDs and (f) LDO/n-CDs electrode at the 1st, 2nd, 5th and 10th cycles between 0.01–3 V at a current density of 100 mA g^{-1}. (g) Cycle performances at the current density of 0.1 A g^{-1}; (h) rate performances at different current densities; (i) Nyquist plots of electrodes.

$$6Ni + Mn + 7Li_2O \rightarrow 6NiO + MnO + 14Li^+ + 14e^- \quad (2)$$

Compared with the subsequent scan, the first scan possesses a wide peak on the broad voltage window and a large capacity loss, indicating a lower initial CE for all electrode.[52–54] It is worthwhile mentioning that, the slight differences between the second, third and fourth CV curves indicate potential cyclic stability. Fig. 8d–f display the galvanostatic charge–discharge curves of LDO, LDO/p-CDs and LDO/n-CDs anode materials for the 1st, 2nd, 5th and 10th cycles at a current density of 100 mA g^{-1}. As one can see, during the discharge process, the curve decline rate is fast above 1.3 V and slow below it, which signifies that more lithium ions are involved in the reaction below 1.3 V.[55,56] During the first charge–discharge process, the charge capacity and discharge capacity of LDO/p-CDs, LDO and LDO/n-CDs electrode are 1619 and 1274 mA h g^{-1}, 1191 and 808 mA h g^{-1}, 1311 and 905 mA h g^{-1}, suggesting an initial CE of 78.7%, 67.9% and 69.1%, respectively. In contrast, the first discharge capacity and the initial CE of LDO/p-CDs are the highest, illustrating the small first capacity attenuation. The apparent loss of the initial circulation capacity is usually attributed to the formation of SEI film at the solid/electrolyte interface.[2,54] Note that the curves overlap well in the subsequent cycles, indicating a good cyclic stability. The results are consistent with the CV results.

Fig. 8g shows the cycling performance of LDO, LDO/p-CDs and LDO/n-CDs electrodes at 0.1 A g^{-1}. It is obvious that the capacity of LDO/p-CDs is highest of them. At a low current density of 0.1 A g^{-1}, the LDO/p-CDs, LDO/n-CDs and LDO electrodes deliver the capacity of 1182 mA h g^{-1}, 882 mA h g^{-1}, 794 mA h g^{-1} after 100 cycles. The coulombic efficiency of LDO, LDO/p-CDs and LDO/n-CDs are 94.9%, 97.9% and 97.4% at the current density of 0.1 A g^{-1} after 100 cycles. It can be observed that the capacity of three electrodes decrease at first and then increase slowly. This may be explained by the reason that due to the unique three-dimensional structure of flowers; a large amount of lithium ions will attach to the active sites of the petals during the process of insertion and extraction, resulting in a decrease in capacity. With the reaction proceeded, the adsorbed lithium ions are released gradually, making the capacity increase. Nevertheless, the capacity of LDO/p-CDs is much higher than that of LDO and LDO/n-CDs. The result implies that the successful synthesis of small size is indeed more conductive to the transport of lithium ions to some extent, which results from a possible explanation that LDO/p-CDs has higher specific surface area, and the diffusion of lithium ions in the internal mesopores increases, resulting in the increase of active sites, meanwhile the small size makes the diffusion channel of lithium ions short, so that lithium ions can diffuse faster. During the cycling process, LDO/p-CDs with small size could release more stress, improve the mechanical stability, and prevent the decline of circulation capacity caused by the collapse of the structure. In order to deeply investigate the electrochemical property of electrodes, we studied rate performance at different current densities over a potential range of 0.01–3 V. As shown in Fig. 8h, LDO/p-CDs display the good capacities of 1156, 1175, 1159, 817, 563 and 282 mA h g^{-1} at the current density of 50, 100, 200, 500, 1000 and 2000 mA g^{-1}, respectively. The capacity can be maintained at 1042 mA h g^{-1} when the current density returns to 50 mA g^{-1}, implying a remarkable rate cycling stability of LDO/p-CDs electrode.

EIS tests were carried out to illustrate the transfer process and diffusion process of lithium ions in the battery. Fig. 8i and inset show the EIS spectrum and equivalent circuit of LDO, LDO/p-CDs and LDO/n-CDs. As can be seen that EIS diagram is composed of a semicircle in the high frequency region (inset of Fig. 8i) and a diagonal line in the low frequency region. The diameter of the semicircle at the high-frequency region represents the charge-transform resistance (R_{ct}) and reflects the conductivity of the electrode materials and electrolyte.[57,58] It can be observed that the semicircle diameter of the LDO/p-CDs electrode ($R_{ct} = 204.2\ \Omega$) in the high frequency range is smaller than LDO, indicating good conductivity and rapid charge transfer.[55,56] It is well known that the closer the phase angles are to 90° at low frequency, the better capacitive performance it represents.[59] The slope of LDO/p-CDs plot is significantly larger than LDO and LDO/n-CDs, indicating that the LDO/p-CDs electrodes perform better. More mesoporous and larger pore volume can provide more active sites in the process of lithium-ion diffusion, and fully contact the electrolyte to accelerate the diffusion rate and reduce the diffusion length. This is consistent with the observation from cycling performance curves.

4. Conclusion

In summary, flower-like LDH/CDs composites composed of nanosheets are successfully prepared by using carbon dots as structure regulator. Among them, LDH/p-CDs with smaller size is derived from the inhibition of the growth of LDH crystals by the chemical characteristics on the surface of p-CDs. After calcination, the LDO/p-CDs possess smaller size, larger specific surface and pore volume compared with LDO, which makes it has remarkable capacity and rate stability as the anode of LIBs. The resultant LDO/p-CDs shows an excellent capacity of 1182 mA h g^{-1} after 100 cycles at the current density of 100 mA g^{-1}. Good cycle stability benefit from stable structure and suppression of volume changes. LDO/p-CDs can increase the contact area of the electrode/electrolyte interface, release stress and improve mechanical stability, while the presence of mesopores allow lithium ions to diffuse faster and provide more active sites. We believe that CDs have more hopeful prospects in the electrochemical energy storage.

Conflicts of interest

There are no conflicts to declare.

Acknowledgements

This project was financially supported by the National Nature Science Foundation of China (21571066, U1501242, 51602107, and 21671069), and the Bureau of Guangdong Forestry (Project No. 2020KJCX008).

References

1 J. S. Wei, H. Ding, P. Zhang, Y. F. Song, J. Chen, Y. G. Wang and H. M. Xiong, Carbon dots/$NiCo_2O_4$ nanocomposites with various morphologies for high performance supercapacitors, *Small*, 2016, **12**, 5927–5934.

2 M. Javed, A. N. S. Saqib, R. Ata ur, B. Ali, M. Faizan, D. A. Anang, Z. Iqbal and S. M. Abbas, Carbon quantum dots from glucose oxidation as a highly competent anode material for lithium and sodium-ion batteries, *Electrochim. Acta*, 2019, **297**, 250–257.

3 M. L. Liu, B. B. Chen, C. M. Li and C. Z. Huang, Carbon dots: synthesis, formation mechanism, fluorescence origin and sensing applications, *Green Chem.*, 2019, **21**, 449–471.

4 S. Y. Lim, W. Shen and Z. Gao, Carbon quantum dots and their applications, *Chem. Soc. Rev.*, 2015, **44**, 362–381.

5 X. Kou, S. Jiang, S. J. Park and L. Y. Meng, A review: recent advances in preparations and applications of heteroatom-doped carbon quantum dots, *Dalton Trans.*, 2020, **49**, 6915–6938.

6 B. Wang, J. Li, Z. Tang, B. Yang and S. Lu, Near-infrared emissive carbon dots with 33.96% emission in aqueous solution for cellular sensing and light-emitting diodes, *Sci. Bull.*, 2019, **64**, 1285–1292.

7 Z. Xu, X. Sun, P. Ma, Y. Chen, W. Pan and J. Wang, A visible-light-excited afterglow achieved by carbon dots from rhodamine B fixed in boron oxide, *J. Mater. Chem. A*, 2020, **8**, 4557–4563.

8 X. Xu, X. Zhang, C. Hu, Y. Zheng, B. Lei, Y. Liu and J. Zhuang, Construction of $NaYF_4$:Yb,Er(Tm)@CDs composites for enhancing red and NIR upconversion emission, *J. Mater. Chem. A*, 2019, **7**, 6231–6235.

9 M. Zheng, Y. Li, S. Liu, W. Wang, Z. Xie and X. Jing, One-pot to synthesize multifunctional carbon dots for near infrared fluorescence imaging and photothermal cancer therapy, *ACS Appl. Mater. Interfaces*, 2016, **8**, 23533–23541.

10 Y. Wang, P. Liu, K. Zhu, J. Wang and J. Liu, Hierarchical bilayered hybrid nanostructural arrays of $NiCo_2O_4$ micro-urchins and nanowires as a free-standing electrode with high loading for high-performance lithium-ion batteries, *Nanoscale*, 2017, **9**, 14979–14989.

11 M. Yuan, Y. Li, Q. Chen, C. Chen, X. Liu, W. Zeng, R. Wang and S. Xiao, Surfactant-assisted hydrothermal synthesis of V_2O_5 coated $LiNi_{1/3}Co_{1/3}Mn_{1/3}O_2$ with ideal electrochemical performance, *Electrochim. Acta*, 2019, **323**, 134822–134828.

12 M. S. Balogun, Y. Luo, F. Lyu, F. Wang, H. Yang, H. Li, C. Liang, M. Huang, Y. Huang and Y. Tong, Carbon quantum dot surface-engineered VO_2 interwoven nanowires: a flexible cathode material for lithium and sodium ion batteries, *ACS Appl. Mater. Interfaces*, 2016, **8**, 9733–9744.

13 Y. Zhang, C. W. Foster, C. E. Banks, L. Shao, H. Hou, G. Zou, J. Chen, Z. Huang and X. Ji, Graphene-rich wrapped petal-like rutile TiO_2 tuned by carbon dots for high-performance sodium storage, *Adv. Mater.*, 2016, **28**, 9391–9399.

14 M. Qing, Y. Meng, Y. Wang, X. Li, C. Zhou, Y. Liang, Z. Zhang, Q. Liu, Y. Guo and D. Xiao, Building nanoparticle-stacking MoO_2-CDs *via in situ* carbon dots reduction as high-performance anode material for lithium ion and sodium ion batteries, *Electrochim. Acta*, 2019, **319**, 740–752.

15 L. Li, R. Li, S. Gai, F. He and P. Yang, Facile fabrication and electrochemical performance of flower-like Fe_3O_4@C@layered double hydroxide (LDH) composite, *J. Mater. Chem. A*, 2014, **2**, 8758–8765.

16 H. S. Jadhav, S. M. Pawar, A. H. Jadhav, G. M. Thorat and J. G. Seo, Hierarchical mesoporous 3D flower-like $CuCo_2O_4$/NF for high-performance electrochemical energy storage, *Sci. Rep.*, 2016, **6**, 31120–31131.

17 J. L. Shi, H. J. Peng, L. Zhu, W. Zhu and Q. Zhang, Template growth of porous graphene microspheres on layered double oxide catalysts and their applications in lithium–sulfur batteries, *Carbon*, 2015, **92**, 96–105.

18 W. Kang, Y. Tang, W. Li, X. Yang, H. Xue, Q. Yang and C. S. Lee, High interfacial storage capability of porous $NiMn_2O_4$/C hierarchical tremella-like nanostructures as the lithium ion battery anode, *Nanoscale*, 2015, **7**, 225–231.

19 A. Bhati, S. R. Anand, Gunture, A. K. Garg, P. Khare and S. K. Sonkar, Sunlight-induced photocatalytic degradation of pollutant dye by highly fluorescent red-emitting Mg-N-embedded carbon dots, *ACS Sustainable Chem. Eng.*, 2018, **6**, 9246–9256.

20 Y. Zhou, D. Benetti, X. Tong, L. Jin, Z. M. Wang, D. Ma, H. Zhao and F. Rosei, Colloidal carbon dots based highly stable luminescent solar concentrators, *Nano Energy*, 2018, **44**, 378–387.

21 W. Li, W. Zhou, Z. Zhou, H. Zhang, X. Zhang, J. Zhuang, Y. Liu, B. Lei and C. Hu, A universal strategy for activating the multicolor room-temperature afterglow of carbon dots in a boric acid matrix, *Angew. Chem., Int. Ed.*, 2019, **58**, 7278–7283.

22 L. Jiang, H. Ding, S. Lu, T. Geng, G. Xiao, B. Zou and H. Bi, Photoactivated fluorescence enhancement in F,N-doped carbon dots with piezochromic behavior, *Angew. Chem., Int. Ed.*, 2020, **59**, 9986–9991.

23 D. Li, W. Li, H. Zhang, X. Zhang, J. Zhuang, Y. Liu, C. Hu and B. Lei, Far-red carbon dots as efficient light-harvesting agents for enhanced photosynthesis, *ACS Appl. Mater. Interfaces*, 2020, **12**, 21009–21019.

24 K. Bhattacharya and P. Deb, Hybrid nanostructured C-dot decorated Fe_3O_4 electrode materials for superior electrochemical energy storage performance, *Dalton Trans.*, 2015, **44**, 9221–9229.

25 Q. Zhang, C. Sun, L. Fan, N. Zhang and K. Sun, Iron fluoride vertical nanosheets array modified with graphene quantum dots as long-life cathode for lithium ion batteries, *Chem. Eng. J.*, 2019, **371**, 245–251.

26 H. Hou, C. E. Banks, M. Jing, Y. Zhang and X. Ji, Carbon quantum dots and their derivative 3D porous carbon frameworks for sodium-ion batteries with ultralong cycle life, *Adv. Mater.*, 2015, **27**, 7861–7866.

27 H. Lv, X. Gao, Q. Xu, H. Liu, Y. G. Wang and Y. Xia, Carbon quantum dot-induced MnO_2 nanowire formation and construction of a binder-free flexible membrane with

excellent superhydrophilicity and enhanced supercapacitor performance, *ACS Appl. Mater. Interfaces*, 2017, **9**, 40394–40403.

28 S. Zhu, Q. Meng, L. Wang, J. Zhang, Y. Song, H. Jin, K. Zhang, H. Sun, H. Wang and B. Yang, Highly photoluminescent carbon dots for multicolor patterning, sensors, and bioimaging, *Angew. Chem., Int. Ed.*, 2013, **125**, 4045–4049.

29 H. Wang, F. Lu, C. Ma, Y. Ma, M. Zhang, B. Wang, Y. Zhang, Y. Liu, H. Huang and Z. Kang, Carbon dots with positive surface charge from tartaric acid and *m*-aminophenol for selective killing of Gram-positive bacteria, *J. Mater. Chem. B*, 2021, **9**, 125–130.

30 J. Zhu, X. Li, Y. Zhang, J. Wang and B. Wei, Graphene-enhanced nanomaterials for wall painting protection, *Adv. Funct. Mater.*, 2018, **28**, 1803872–1803881.

31 Y. Ouyang, Y. Feng, H. Zhang, L. Liu and Y. Wang, Designing sandwiched and crystallized $NiMn_2O_4$/C arrays for enhanced sustainable electrochemical energy storage, *ACS Sustainable Chem. Eng.*, 2016, **5**, 196–205.

32 L. Shi, Y. Chen, H. Song, A. Li, X. Chen, J. Zhou and Z. Ma, Preparation and lithium-storage performance of a novel hierarchical porous carbon from sucrose using Mg–Al layered double hydroxides as template, *Electrochim. Acta*, 2017, **231**, 153–161.

33 G. Yilmaz, K. M. Yam, C. Zhang, H. J. Fan and G. W. Ho, *In situ* transformation of MOFs into layered double hydroxide embedded metal sulfides for improved electrocatalytic and supercapacitive performance, *Adv. Mater.*, 2017, **29**, 1606814–1606821.

34 X. He, R. Li, J. Liu, Q. Liu, R. chen, D. Song and J. Wang, Hierarchical $FeCo_2O_4$@NiCo layered double hydroxide core/shell nanowires for high performance flexible all-solid-state asymmetric supercapacitors, *Chem. Eng. J.*, 2018, **334**, 1573–1583.

35 Y. Liu, N. Fu, G. Zhang, M. Xu, W. Lu, L. Zhou and H. Huang, Design of hierarchical Ni–Co@Ni–Co layered double hydroxide core–shell structured nanotube array for high-performance flexible all-solid-state battery-type supercapacitors, *Adv. Funct. Mater.*, 2017, **27**, 1605307–1605317.

36 S. Liu, S. C. Lee, U. Patil, I. Shackery, S. Kang, K. Zhang, J. H. Park, K. Y. Chung and S. Chan Jun, Hierarchical MnCo-layered double hydroxides@$Ni(OH)_2$ core–shell heterostructures as advanced electrodes for supercapacitors, *J. Mater. Chem. A*, 2017, **5**, 1043–1049.

37 J. Lin, H. Jia, H. Liang, S. Chen, Y. Cai, J. Qi, C. Qu, J. Cao, W. Fei and J. Feng, Hierarchical $CuCo_2S_4$@NiMn-layered double hydroxide core–shell hybrid arrays as electrodes for supercapacitors, *Chem. Eng. J.*, 2018, **336**, 562–569.

38 B. Hou, Y. Du, X. Liu, C. Ci, X. Wu and X. Xie, Tunable preparation of highly dispersed Ni_xMn–LDO catalysts derived from Ni_xMn–LDHs precursors and application in low-temperature NH_3-SCR reactions, *RSC Adv.*, 2019, **9**, 24377–24385.

39 L. Huang, B. Liu, H. Hou, L. Wu, X. Zhu, J. Hu and J. Yang, Facile preparation of flower-like NiMn layered double hydroxide/reduced graphene oxide microsphere composite for high-performance asymmetric supercapacitors, *J. Alloys Compd.*, 2018, **730**, 71–80.

40 Y. Zhang, C. Huang, H. Min, H. Shu, P. Gao, Q. Liang, X. Yang, L. Liu and X. Wang, Bowl-like double carbon layer architecture of hollow carbon@$FePO_4$@reduced graphene oxide composite as high-performance cathodes for sodium and lithium ion batteries, *J. Alloys Compd.*, 2019, **795**, 34–44.

41 A. Sumboja, J. Chen, Y. Zong, P. S. Lee and Z. Liu, NiMn layered double hydroxides as efficient electrocatalysts for the oxygen evolution reaction and their application in rechargeable Zn–air batteries, *Nanoscale*, 2017, **9**, 774–780.

42 Y. Xia, G. Wang, X. Zhang, B. Wang and H. Wang, General access to metal oxide (Metal = Mn, Co, Ni) double-layer nanospheres for application in lithium ion batteries and supercapacitors, *Electrochim. Acta*, 2016, **220**, 643–653.

43 J. Zhou, M. Min, Y. Liu, J. Tang and W. Tang, Layered assembly of NiMn-layered double hydroxide on graphene oxide for enhanced non-enzymatic sugars and hydrogen peroxide detection, *Sens. Actuators, B*, 2018, **260**, 408–417.

44 X. Li, D. Du, Y. Zhang, W. Xing, Q. Xue and Z. Yan, Layered double hydroxides toward high-performance supercapacitors, *J. Mater. Chem. A*, 2017, **5**, 15460–15485.

45 J. Zhang, K. Xiao, T. Zhang, G. Qian, Y. Wang and Y. Feng, Porous nickel–cobalt layered double hydroxide nanoflake array derived from ZIF-L-Co nanoflake array for battery-type electrodes with enhanced energy storage performance, *Electrochim. Acta*, 2017, **226**, 113–120.

46 X. Wang, Q. Wang, X. Hou, Y. Liu, P. Zheng, J. Huo, L. Yin and S. Guo, Facile fabrication of two-dimensional reduced graphene oxide/CoAl-layered double hydroxides nanocomposites for lithium–oxygen battery with improved electrochemical performance, *J. Alloys Compd.*, 2018, **744**, 196–203.

47 J. Chen, S. Li, K. Qian and P. S. Lee, NiMn layered double hydroxides derived multiphase Mn-doped Ni sulfides with reduced graphene oxide composites as anode materials with superior cycling stability for sodium ion batteries, *Mater. Today Energy*, 2018, **9**, 74–82.

48 L. Yang, H. Li, S. Zhang, F. Yao, J. Lv and S. Xu, Novel layered double hydroxide precursor derived high-Co_9S_8-content composite as anode for lithium-ion batteries, *J. Alloys Compd.*, 2018, **768**, 485–494.

49 J. Li, C. Shu, Z. Ran, M. Li, R. Zheng and J. Long, Heteroatom-induced electronic structure modulation of vertically oriented oxygen vacancy-rich NiFe layered double oxide nanoflakes to boost bifunctional catalytic activity in Li–O_2 battery, *ACS Appl. Mater. Interfaces*, 2019, **11**, 29868–29878.

50 H. Chen, X. Chang, D. Chen, J. Liu, P. Liu, Y. Xue, H. Lin and S. Han, Graphene-karst cave Flower-like Ni–Mn layered double oxides nanoarrays with energy storage electrode, *Electrochim. Acta*, 2016, **220**, 36–46.

51 M. Latorre-Sanchez, P. Atienzar, G. Abellán, M. Puche, V. Fornés, A. Ribera and H. García, The synthesis of a hybrid graphene–nickel/manganese mixed oxide and its performance in lithium-ion batteries, *Carbon*, 2012, **50**, 518–525.

52 S. Liu, X. Zhang, S. Wu, X. Chen, X. Yang, W. Yue, J. Lu and W. Zhou, Crepe cake structured layered double hydroxide/

sulfur/graphene as a positive electrode material for Li-S batteries, *ACS Nano*, 2020, **14**, 8220–8231.

53 L. Wu, J. Lang, S. Wang, P. Zhang and X. Yan, Study of Ni-dopped $MnCo_2O_4$ yolk–shell submicron-spheres with fast Li^+ intercalation pseudocapacitance as an anode for high-performance lithium ion batteries, *Electrochim. Acta*, 2016, **203**, 128–135.

54 W. Hong, Y. Zhang, L. Yang, Y. Tian, P. Ge, J. Hu, W. Wei, G. Zou, H. Hou and X. Ji, Carbon quantum dot micelles tailored hollow carbon anode for fast potassium and sodium storage, *Nano Energy*, 2019, **65**, 104038–104049.

55 S. Zhang, F. Yao, L. Yang, F. Zhang and S. Xu, Sulfur-doped mesoporous carbon from surfactant-intercalated layered double hydroxide precursor as high-performance anode nanomaterials for both Li-ion and Na-ion batteries, *Carbon*, 2015, **93**, 143–150.

56 L. Shi, Y. Chen, R. He, X. Chen and H. Song, Graphene-wrapped CoNi-layered double hydroxide microspheres as a new anode material for lithium-ion batteries, *Phys. Chem. Chem. Phys.*, 2018, **20**, 16437–16443.

57 Q. Li, Y. Wang, B. Lu, J. Yu, M. Yuan, Q. Tan, Z. Zhong and F. Su, Hollow core–shell structured Si@NiAl–LDH composite as high-performance anode material in lithium-ion batteries, *Electrochim. Acta*, 2020, **331**, 135331–135357.

58 L. Shi, Y. Chen, G. Chen, Y. Wang, X. Chen and H. Song, Fabrication of hierarchical porous carbon microspheres using porous layered double oxide templates for high-performance lithium ion batteries, *Carbon*, 2017, **123**, 186–192.

59 G. Yuan, H. Li, H. Hu, Y. Xie, Y. Xiao, H. Dong, Y. Liang, Y. Liu and M. Zheng, Microstructure engineering towards porous carbon materials derived from one biowaste precursor for multiple energy storage applications, *Electrochim. Acta*, 2019, **326**, 134974–135003.